J. Fluid Mech. (2003), *vol.* 497, *pp.* 235–252. © 2003 Cambridge University Press
DOI: 10.1017/S0022112003006621 Printed in the United Kingdom

Motion and shape of a viscoelastic drop falling through a viscous fluid

By MICHAEL C. SOSTARECZ AND ANDREW BELMONTE

The W. G. Pritchard Laboratories, Department of Mathematics, Pennsylvania State University, University Park, PA 16802, USA

(Received 3 January 2003 and in revised form 15 August 2003)

The steady shape of a drop of dilute polymer solution falling through a quiescent viscous Newtonian fluid is considered. Experimentally, we find that an immiscible drop of 0.16% xanthan gum in 80:20 glycerol/water falling through 9.8 P polydimethylsiloxane oil may exhibit a stable dimple at its trailing edge. At higher volumes the dimple extends far into the interior of the drop, and pinches off via a Rayleigh-type instability, injecting oil droplets into the polymer drop. At even larger volumes, a toroidal shape develops. We show that the dimpled shape can be reproduced mathematically with axisymmetric solutions for Stokes flow past a non-Newtonian drop, using the constitutive equation for a Simple Fluid of Order Three.

1. Introduction

Among the instabilities that differentiate viscoelastic or non-Newtonian fluid flows from Newtonian (Navier–Stokes) flows, those involving free surfaces are among the most striking (see e.g. Larson 1992; Boger & Walters 1993). Specific examples include filament beads (Goldin *et al.* 1969), die swell and sharkskin instabilities (Venet & Vergnes 1997), and the apparent cusp at the trailing end of a rising bubble (Hassager (1979); Liu, Liao & Joseph 1995). In each of these well-known cases the interface separates a non-Newtonian fluid, typically a polymer melt or solution, from air. The cusp-like tail is a particularly surprising steady-state shape, which implies that stresses in the wake of the bubble are very high. Generally, the motion and shape of an axisymmetric immiscible liquid drop under gravity has become a benchmark problem in fluid dynamics, which like the deformation of a drop in a four-roll mill, has led to many important results in the competition between fluid stresses and surface tension (Taylor 1934; Stone 1994). For a small enough falling drop, surface tension effects dominate, and the shape is spherical. As the volume of the drop is increased, the curvature of the sphere is reduced, and the drop falls faster. The free surface then deforms from its spherical shape in response to the forces (pressure and internal stresses) in the flowing fluid.

Of the mathematical approaches which have been taken on the drop problem, most have focused on the limiting cases of an air bubble or a solid sphere translating through an infinite non-Newtonian fluid. Analytically, the non-Newtonian fluid is often modelled by one of the ordered 'simple fluids' (Bird, Armstrong & Hassager 1987). An Order Three fluid has been used to solve the flow around a rigid sphere (Caswell & Schwarz 1962) and to obtain the approximate shape of a rising air bubble (Tiefenbruck & Leal 1980). The general case of an Order Three fluid drop falling in

https://doi.org/10.1017/S0022112003006621 Published online by Cambridge University Press

another Order Three fluid was considered by Wagner & Slattery (1971). For a more complete overview and history, see Dairenieh & McHugh (1985).

In this paper we present an experimental study of the steady-state shape of a single non-Newtonian drop falling through a viscous Newtonian fluid. While this particular geometry and arrangement has been considered before mathematically (Ramkissoon 1989, 1998), to our knowledge this is the first experimental study. We find that, at a critical drop volume, the free surface develops an *inward dimple* at its rear stagnation point. This transition is similar to the dimple produced by inertial effects in Newtonian drops (Garner, Mathur & Jenson 1957); however, the deformation we observe is not due to inertia, confirmed by the spherical shape of the same drop without the polymer. Our observations provide another example of a non-Newtonian effect at negligible Reynolds number which mimics an inertial instability (Shaqfeh 1996). At high enough volumes this indentation becomes unstable to an interior pinch-off, leading to many small droplets of the solvent which fill the large drop. These shapes are remarkably similar to some of the transients seen by Leal and coworkers in Newtonian fluids (Koh & Leal 1990). We perform a formal expansion in the non-dimensional relaxation time (Deborah number De) and surface tension (capillary number Ca), which we treat as an *ad hoc* model for our observations, as we will truncate at third order in the small quantities. This approach allows us to qualitatively reproduce our experimental findings.

2. Experimental observations

2.1. *Apparatus and fluids*

Our experimental setup consists of a clear rectangular cell filled with 9.8 P polydimethylsiloxane (PDMS) oil. The cell is a Plexiglas box, 42 cm in height, with cross-sectional area of 5.7 cm $\times$ 6.3 cm. A drop of polymer solution is introduced at the top of the cell as a roughly spherical globule, either injected from a precision syringe for the smaller volumes (§ 2.3 and § 2.4), or poured from a beaker for the larger volumes (§ 2.5); the details of this initial shape do not affect the final drop shape. The drop is allowed to fall approximately 33 cm before being observed (at which time it has reached steady state). The drops range in size from 0.01 ml to 1.5 ml, for which $d/D \leqslant 0.2$, where d is the horizontal diameter of the drop, and D is the narrower width of the cell. The shape and speed of the drop are recorded with a video camera (COHU 4912) and a digital image processing system (NIH Image on a Macintosh G3, with a Scion AG-5 frame grabber). All experimental data were taken at room temperature, which was controlled at 25 °C.

The drop phase is a polymer solution of 0.16% xanthan gum† by weight in 80:20 glycerol/water by volume (Smolka & Belmonte 2000). It has density $\tilde{\rho} = 1.27\,\mathrm{g\,cm^{-3}}$, whereas the exterior oil has $\rho = 0.98\,\mathrm{g\,cm^{-3}}$. A surface tension between the two fluids of $\Gamma = 25\,\mathrm{dyn\,cm^{-1}}$ was measured by a pendant drop technique, using the procedure outlined by Ambwani & Fort (1979). Xanthan gum is a high-molecular-weight ($\approx 2 \times 10^6$), water-soluble, anionic polysaccharide produced by the bacterium *Xanthomonas Campestris* (Whitcomb & Macosko 1978; Nussinovitch 1997). The xanthan gum was mixed at low heat into an 80:20 (by volume) glycerol and distilled deionized water solution, using an industrial electric mixer (Eastern mixers, Model No. 8A-RS) at rates between 30 and 120 r.p.m. After one day of mixing the fluids

† Vanzan NF, provided by R.T. Vanderbilt Co. (Norwalk, CT).

https://doi.org/10.1017/S0022112003006621 Published online by Cambridge University Press

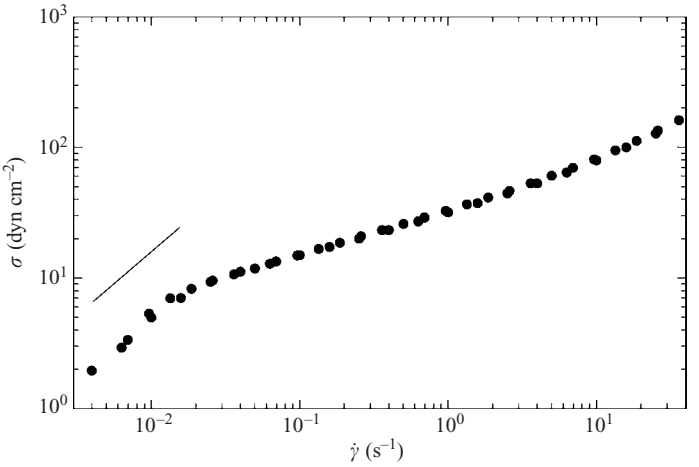


FIGURE 1. The steady shear stress vs. the applied shear rate, for the solution of 0.16% xanthan gum in 80:20 glycerol/water at 25 °C. The line shows the Newtonian scaling $\sigma \sim \dot{\gamma}$.

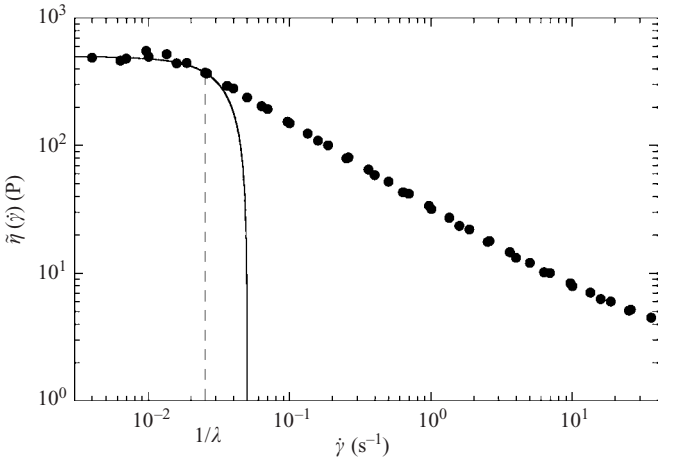


FIGURE 2. The apparent shear viscosity of the solution of 0.16% xanthan gum in 80:20 glycerol/water at 25 °C. An approximation of the relaxation time λ is obtained from the shear rate at which $\tilde{\eta}(\dot{\gamma})$ thins below $\tilde{\eta}_0$ (dashed line). The solid line corresponds to a theoretical fit with (3.5) as discussed in § 3.2.

were homogeneous. The solutions were set aside for two weeks before being used in experiments.

2.2. *Rheology of the interior fluid*

Rheological measurements of the xanthan gum solution were performed with a temperature-controlled Rheometrics RFS-III rheometer, in strain-controlled mode. The fluid was tested in a standard Couette cell at $T = 25\,^{\circ}\mathrm{C}$, with an inner cylinder of diameter 32 mm and height 33 mm, and with a gap of 1 mm.

We measure the steady shear stress σ as a function of applied shear rate $\dot{\gamma}$, as shown in figure 1. We also plot the apparent shear viscosity $\tilde{\eta}(\dot{\gamma}) \equiv \sigma/\dot{\gamma}$ in figure 2. This indicates that the fluid is shear thinning, with a zero shear viscosity $\tilde{\eta}_0 \simeq 500$ P. In the shear-thinning region, we find a power law dependence $\tilde{\eta}(\dot{\gamma}) \sim \dot{\gamma}^{\beta}$, with $\beta = -0.63$

https://doi.org/10.1017/S0022112003006621 Published online by Cambridge University Press

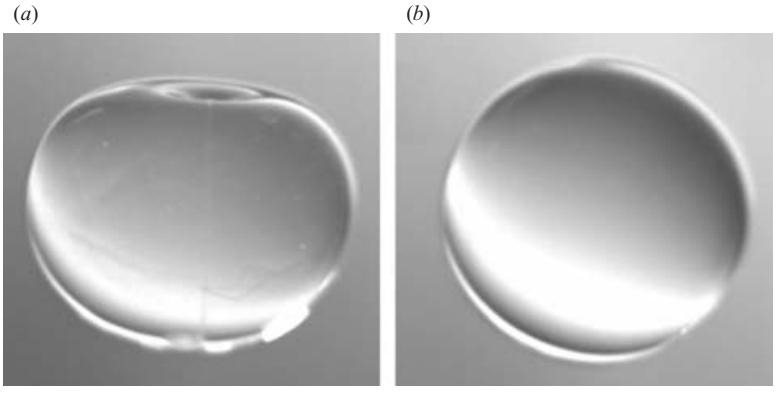


FIGURE 3. Two 0.73 ml drops falling through 9.8 P polydimethylsiloxane (PDMS) oil: (*a*) 0.16% xanthan gum/80:20 glycerol/water; (*b*) 80:20 glycerol/water.

(not shown). One estimate of the relaxation time λ is to take the inverse of the shear rate where $\tilde{\eta}(\dot{\gamma})$ thins below $\tilde{\eta}_0$. Using this, we find $\lambda \simeq 40$ s.

2.3. *Transition to a dimpled drop*

The steady shape and velocity of a polymer drop falling through a quiescent viscous Newtonian fluid is determined by a balance of the net gravitational force, external viscous stresses, pressure, surface tension, and internal viscoelastic stresses. The relative importance of these various effects can be characterized by several non-dimensional parameters. Taking the equivalent radius $R = (3\mathrm{Vol}/4\pi)^{1/3}$ and terminal velocity U_∞ of the drop as the characteristic length and velocity scales, respectively, we define the Reynolds and capillary numbers of the external fluid as

$$Re = \frac{\rho R U_\infty}{\eta}, \qquad Ca = \frac{\eta U_\infty}{\Gamma},$$

and the Deborah number of the interior as

$$De = \frac{\lambda U_0}{R}.$$

Here U_0 is a typical interior flow speed, which we choose *a priori* to be $U_0 = U_\infty/(\kappa+1)$, where $\kappa = \tilde{\eta}_0/\eta$ (this choice will be explained in § 3.4). For our experiments, $\kappa = 50$.

When a xanthan drop is allowed to fall through a viscous oil, an inward cusp is observed, as shown in figure 3(*a*). In fact, the shape bears some resemblance to the well-known cusped air bubble rising through a polymer solution (Hassager 1979; Liu *et al.* 1995); here the cusp-like extension of the surface is also drawn into the non-Newtonian phase, as one would expect from applying an inversion mapping to the cusped air bubble, putting the non-Newtonian fluid inside, and the Newtonian fluid outside. The drop falls at a terminal velocity of 1.1 cm s^{-1}, which means that the exterior flow has a Reynolds number of $Re \simeq 6 \times 10^{-2}$ (using the volume equivalent radius of $R = 0.56$ cm). Using the relaxation time $\lambda \simeq 40$ s from the rheology of the interior phase, we find a Deborah number of $De \simeq 1.5$. We therefore attribute the dimpled shape to the elasticity of the interior fluid.

A dimpled drop shape similar to figure 3(*a*) occurs due to inertial effects (Garner *et al.* 1957; Wellek, Agrawal & Skelland 1966), and in fact the mathematics of the perturbations due to elastic effects presented below are similar to the inclusion of inertial effects (Taylor & Acrivos 1964). In the opposite (viscous) limit, a striking

https://doi.org/10.1017/S0022112003006621 Published online by Cambridge University Press

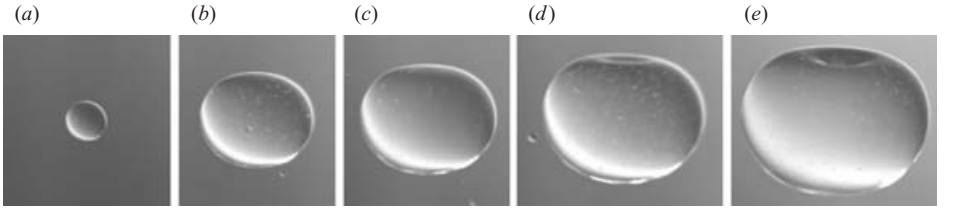


FIGURE 4. Steady-state shapes of xanthan drops falling through 9.8 P oil. The drop volumes shown are (*a*) 0.01 ml, (*b*) 0.12 ml, (*c*) 0.21 ml, (*d*) 0.35 ml, and (*e*) 0.52 ml.

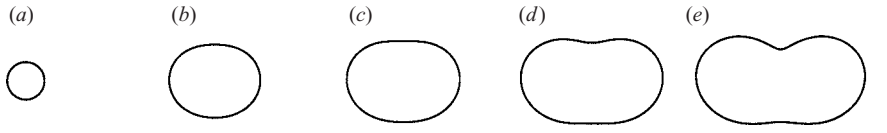


FIGURE 5. Calculated steady-state axisymmetric shapes of Order Three drops falling through Stokes fluid. The drop volumes shown are (*a*) 0.01 ml, (*b*) 0.12 ml, (*c*) 0.21 ml, (*d*) 0.35 ml, and (*e*) 0.52 ml. These calculated shapes correspond to the theoretical prediction given in (3.25).

instability to a growing dimple has been seen for a Newtonian drop falling through an ambient Newtonian fluid; this large and transient distortion results from either a finite initial perturbation or the absence of surface tension, and has been observed both experimentally (Koh & Leal 1990) and numerically (Koh & Leal 1989; Pozrikidis 1990). In contrast, our dimpled drops are steady in shape, occurring without any strong initial perturbation and in the presence of significant surface tension.

To confirm that our observations can be attributed to elastic effects alone, we observed that a falling viscous Newtonian drop of the same volume (0.73 ml) has a spherical shape, as shown in figure 3(*b*); the fluid used is the pure solvent, 80:20 glycerol/water, without any added polymer. While the terminal velocity in this case ($1.6\,\mathrm{cm\,s^{-1}}$) is not far from that of the polymer drop, the shape is quite different. The lower terminal velocity of the slightly heavier and effectively more viscous polymer drop cannot be fully accounted for by the dependence of the classical terminal velocity on density and viscosity (Happel & Brenner 1965), which would predict only a small decrease (less than 5%). The rest of the observed 30% decrease must be due to either shape or elastic effects.

To observe the onset of this instability, we varied the drop size. For small enough volumes, the xanthan drop falls slowly and is spherical, as shown in figure 4(*a*) (0.01 ml). For volumes from 0.05 to 0.24 ml, the drop has an oblate spheroidal shape. At a critical volume of 0.25 ml, a dimple is observed at the rear of the drop (the critical volume is between (*c*) and (*d*) in figure 4). In § 3, we model the drop phase as a Simple Fluid of Order Three to mathematically obtain the drop's shape. These results are shown in figure 5.

The changes in the shape of the drop and the flow of the non-Newtonian fluid inside will also affect the drag on the drop as it falls, and therefore its terminal velocity. In figure 6 we plot the terminal velocity of the polymer drop, measured after the drop has fallen through 30 cm of the viscous fluid. The velocity is shown as a function of the equivalent radius. The two theoretical predictions shown with the data are discussed in § 3.10.

https://doi.org/10.1017/S0022112003006621 Published online by Cambridge University Press

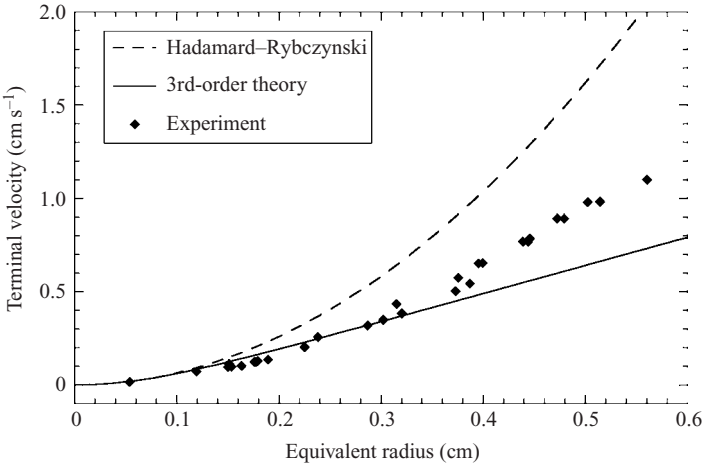


FIGURE 6. Terminal velocity vs. equivalent radius. The dashed and solid lines correspond to the theoretical predictions given in (3.14) and (3.26) respectively.

2.4. *Interior filament and droplet generation*

For drop volumes above about 1 ml, the dimple becomes unstable. The exterior fluid is pulled down into the drop, and resembles a falling pendant drop followed by a filament (figure 7*a*). However, in this case the pendant oil drop is *lighter* than the surrounding polymer fluid. The filament becomes unstable to breakup inside the polymer drop (figure 7*b*), which bears a striking resemblance to the classic Rayleigh instability (Shi, Brenner & Nagel 1994; Eggers 1997).

After the pinch-off of the pendant drop, the internal cusp that remains becomes unstable to a 'tip-streaming' instability (Taylor 1934; Milliken & Leal 1991), and the xanthan drop begins to fill with smaller oil drops. This indicates that the stresses generated by the non-Newtonian fluid inside the drop have overcome the surface tension forces, resulting in the injection of fluid into the interior, similar to the transition seen by Jeong & Moffatt (1992) in viscous Newtonian fluids.

2.5. *Torus formation*

Here a slightly different experimental setup was used to view some larger drop sizes, ranging between 5.0 ml and 15.0 ml. Due to the size of the drops and the time required to reach a steady-state shape, we used a larger rectangular cell, with cross-section 7.5 cm × 9.0 cm and height 120 cm, filled with 4.9 P PDMS oil. The drops were viewed approximately 80 cm down the cell (at which time the drops were in steady state).

For these larger volumes, the filament of oil pulled into the polymer drop becomes wider and more stable. The filament extends down to the leading edge of the drop, resulting in the formation of a new dimple. Eventually the front and back dimples coalesce, making a toroidal drop as shown in figure 7(*c*). This process often results in the pinch-off of the pendant oil drop, which is pushed off to the side.

There are several examples of toroidal bubbles and drops in the literature. For instance, as two immiscible Newtonian drops fall through a viscous Newtonian oil, the leading drop will, under some conditions, form a torus due to its interactions with the second drop (Kushner, Rother & Davis 2001). Toroidal bubbles have also been observed in cavitation processes near walls (see e.g. Benjamin & Ellis 1966). Walters

https://doi.org/10.1017/S0022112003006621 Published online by Cambridge University Press

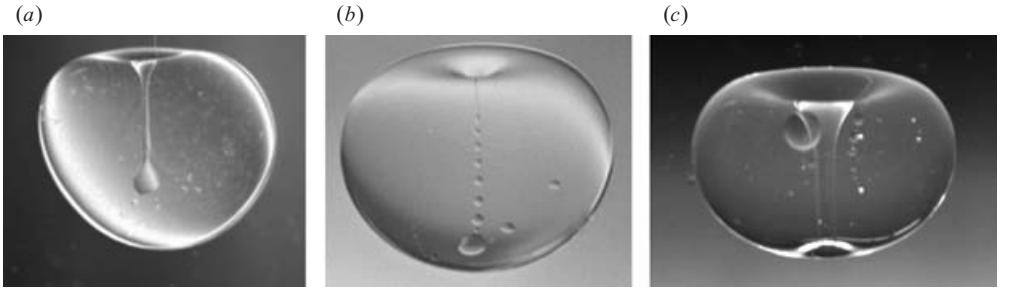


FIGURE 7. Shape transitions for larger polymer drops. Volumes shown are (*a*) 1.4 ml; (*b*) 1.5 ml; (*c*) 7.0 ml (torus).

& Davidson (1963) were able to create a toroidal bubble by rapidly opening and closing an air jet at the bottom of a water tank. Remarkably, some dolphins at play will form similar toroidal bubbles by blowing air into a vortex they produce with their tail (Marten *et al.* 1996).

Toroidal shapes have also been seen experimentally for a single falling drop in Newtonian fluids when the two fluids are miscible (Kojima, Hinch & Acrivos 1984; Machu *et al.* 2001) or have very low surface tension (Baumann *et al.* 1992). In the experiments of Baumann *et al.*, viscous effects alone overpowered the surface tension forces (at high Ca) resulting in the toroidal shape. Without any force working against viscous dissipation, the torus they observed 'rapidly expanded' until breaking into smaller drops. In contrast to all of the above experiments, the toroidal polymer drops studied here appear to be stable, and are not observed to expand or contract over a distance of 30 cm (at which point they reach the bottom of the cell).

3. Mathematical description

To mathematically describe the elastic effects we observe in a falling polymer drop, we take a perturbative approach to the drop shape, using the axisymmetric Hadamard–Rybczynski solution as our base flow. There have been many similar mathematical studies for a variety of cases, as discussed above. Our approach can be viewed as a special case of Wagner & Slattery (1971), in that the Rivlin–Eriksen constitutive equation they use is formally equivalent to the one used here. Using the retarded motion expansion for the dependence of the stress tensor on velocity gradients (Bird *et al.* 1987), we can reproduce the shape transitions shown in figure 4. In so doing, we represent the exterior flow with the Stokes equation, i.e. $Re = 0$. This is an approximation, as it is well-known that setting $Re = 0$ is inconsistent with any small Re in the Navier–Stokes equation (Batchelor 1967).

3.1. *Statement of the mathematical problem*

To calculate the effects of non-Newtonian stresses on the shape of a falling drop, we assume first that the flow remains axisymmetric, and we treat only the steady (time-independent) case. We assume that inertial effects are negligible for both fluids. The exterior fluid is Newtonian and incompressible, and thus is described by the steady Stokes equation:

$$\left.\begin{aligned} &\nabla \cdot \boldsymbol{u} = 0, \\ &\nabla p = \nabla \cdot \boldsymbol{\tau} + \rho \boldsymbol{g}, \\ &\boldsymbol{\tau} = 2\eta \boldsymbol{D}, \end{aligned}\right\} \tag{3.1}$$

https://doi.org/10.1017/S0022112003006621 Published online by Cambridge University Press

where $\boldsymbol{D} = (\nabla \boldsymbol{u} + \nabla \boldsymbol{u}^T)/2$ is the symmetric part of the velocity gradient tensor (the deformation tensor), $\boldsymbol{\tau}$ the extra stress tensor, $\boldsymbol{u}$ the velocity field, p the pressure, $\boldsymbol{g}$ the gravitational acceleration, η the viscosity, and ρ the density.

The definition of a non-Newtonian fluid is simply a fluid which does not obey the Navier–Stokes equation. The interior fluid is modelled as a Simple Fluid of Order Three, which is an expansion of the functional dependence of the stress tensor on the deformation gradient tensor and its proper tensor derivatives; this equation is exact as $De \to 0$ (Bird *et al.* 1987). Denoting the interior-fluid variables with tildes, the governing equations are

$$\left.\begin{aligned} \nabla \cdot \tilde{\boldsymbol{u}} &= 0, \\ \nabla \tilde{p} &= \nabla \cdot \tilde{\boldsymbol{\tau}} + \tilde{\rho} \boldsymbol{g}, \end{aligned}\right\} \tag{3.2}$$

where the constitutive equation for $\tilde{\boldsymbol{\tau}}$ is given by

$$\tilde{\boldsymbol{\tau}} = 2b_1 \tilde{\boldsymbol{D}} + 2b_2 \hat{\mathrm{d}} \tilde{\boldsymbol{D}} + 4b_{11} \tilde{\boldsymbol{D}} \cdot \tilde{\boldsymbol{D}} + 2b_3 \hat{\mathrm{d}}^2 \tilde{\boldsymbol{D}} + 4b_{12} (\tilde{\boldsymbol{D}} \cdot \hat{\mathrm{d}} \tilde{\boldsymbol{D}} + \hat{\mathrm{d}} \tilde{\boldsymbol{D}} \cdot \tilde{\boldsymbol{D}}) + 8b_{1:11} (\tilde{\boldsymbol{D}} : \tilde{\boldsymbol{D}}) \tilde{\boldsymbol{D}} \tag{3.3}$$

and the operator $\hat{\mathrm{d}}$ is the upper convected tensor derivative (Bird *et al.* 1987)

$$\hat{\mathrm{d}}(\cdot) = \left(\frac{\partial}{\partial t} + \tilde{\boldsymbol{u}} \cdot \nabla \right) (\cdot) - \nabla \tilde{\boldsymbol{u}}^T (\cdot) - (\cdot) \nabla \tilde{\boldsymbol{u}}. \tag{3.4}$$

The six parameters $b_1, b_2, b_{11}, b_3, b_{12}, b_{1:11}$ are the retarded motion constants, which are related to the rheological constants of the fluid, as discussed in § 3.2.

The steady-state boundary conditions at the interface require that the normal velocity components are zero and the tangential components are continuous. Also at the interface, we have that the tangential components of the stresses are equal while the difference in the normal components of the stress is equal to the surface tension of the interface Γ times its curvature (Batchelor 1967): $-p + \boldsymbol{n} \cdot \boldsymbol{\tau} \cdot \boldsymbol{n} = -\tilde{p} + \boldsymbol{n} \cdot \tilde{\boldsymbol{\tau}} \cdot \boldsymbol{n} + \Gamma(1/R_1 + 1/R_2)$, where $\boldsymbol{n}$ is the unit vector normal to the droplet surface, and R_1, R_2 are the principle radii of curvature. We assume the drop is falling in an infinite bath with the origin of our coordinate system fixed at the drop's centre of mass. At infinity, the flow is assumed to be free streaming with velocity U_∞ in the vertical direction. Finally, it makes sense physically to require finite flow speeds everywhere.

3.2. *Rheology of an Order Three fluid*

We recall here some standard results for the rheology of a Simple Fluid of Order Three (Bird *et al.* 1987). Inserting the constitutive equation (3.3) into a simple shear flow in Cartesian coordinates $[\boldsymbol{u}]_x = \dot{\gamma} y$, we obtain the shear stress $\sigma = [\boldsymbol{\tau}]_{xy}$ as

$$\sigma = b_1 \dot{\gamma} + b_2 \frac{\partial \dot{\gamma}}{\partial t} + b_3 \frac{\partial^2 \dot{\gamma}}{\partial t^2} - 2(b_{12} - b_{1:11}) \dot{\gamma}^3.$$

For steady shear, this becomes $\sigma = b_1 \dot{\gamma} - 2(b_{12} - b_{1:11}) \dot{\gamma}^3$ from which the apparent viscosity is defined to be

$$\tilde{\eta}(\dot{\gamma}) \equiv \frac{\sigma(\dot{\gamma})}{\dot{\gamma}} = b_1 - 2(b_{12} - b_{1:11}) \dot{\gamma}^2. \tag{3.5}$$

Thus, the zero shear viscosity $\tilde{\eta}_0 = b_1$, and for shear thinning we must have $b_{12} > b_{1:11}$. Fitting the experimentally observed apparent viscosity with (3.5) to capture the onset of shear thinning, we find that $\tilde{\eta}_0 = 500\,\mathrm{P}$ and $b_{12} - b_{1:11} = 10^5\,\mathrm{P\,s^2}$ (see figure 2). Unlike what was seen experimentally, the apparent viscosity in this model does not have

https://doi.org/10.1017/S0022112003006621 Published online by Cambridge University Press

Parameter:	$\tilde{\eta}_0$	λ	B_{11}	B_3	B_{12}	$B_{1:11}$
Value:	500 P	40 s	0.41	1.20	0.44	0.32

TABLE 1. Values of parameters used in Third Order fluid equation.

a power law dependence at high shear rates. We have therefore only qualitatively included shear-thinning effects (note that an Order Two fluid does not shear thin).

Computing the normal stress coefficients, it is found that the first normal stress coefficient is $b_2 = -\Psi_{1,0}/2$, and the second normal stress coefficient is $b_{11} = \Psi_{2,0}$. From this, we define our relaxation time to be $\lambda = -b_2/b_1 = \Psi_{1,0}/2\tilde{\eta}_0$; we use $\lambda = 40\,\mathrm{s}$, as obtained in § 2.2.

3.3. *Elastic perturbations at nonzero Deborah number*

We consider a formal perturbation expansion of the flow variables in Deborah number De, taken to second order, similar to the small-Re study by Taylor & Acrivos (1964). Although we non-dimensionalize all lengths by R, we choose different velocity and stress scales in the exterior and interior: in the exterior our scales are U_∞ and $\eta U_\infty/R$, while in the interior we choose U_0 and $\tilde{\eta}_0 U_0/R$. These scales are related since $U_0 = U_\infty/(\kappa+1)$ and $\tilde{\eta}_0 = \kappa\eta$. Under these choices the constitutive equation and the normal stress boundary condition become

$$\begin{aligned}\tilde{\boldsymbol{\tau}} &= 2\tilde{\boldsymbol{D}} - De(2\hat{\mathrm{d}}\tilde{\boldsymbol{D}} + 4B_{11}\tilde{\boldsymbol{D}}\cdot\tilde{\boldsymbol{D}}) \\ &\quad + De^2(2B_3\hat{\mathrm{d}}^2\tilde{\boldsymbol{D}} + 4B_{12}(\tilde{\boldsymbol{D}}\cdot\hat{\mathrm{d}}\tilde{\boldsymbol{D}} + \hat{\mathrm{d}}\tilde{\boldsymbol{D}}\cdot\tilde{\boldsymbol{D}}) + 8B_{1:11}(\tilde{\boldsymbol{D}}:\tilde{\boldsymbol{D}})\tilde{\boldsymbol{D}})\end{aligned} \tag{3.6}$$

and

$$\boldsymbol{n}\cdot\left(\boldsymbol{\tau} - \frac{\kappa}{\kappa+1}\tilde{\boldsymbol{\tau}}\right)\cdot\boldsymbol{n} - p + \tilde{p} = \frac{1}{Ca}\left(\frac{1}{R_1} + \frac{1}{R_2}\right). \tag{3.7}$$

Here we have modified the constitutive parameters following the standard normalization (Bird *et al.* 1987): $B_{11} = -b_{11}/\lambda\tilde{\eta}_0$, $B_3 = b_3/\lambda^2\tilde{\eta}_0$, $B_{12} = b_{12}/\lambda^2\tilde{\eta}_0$, and $B_{1:11} = b_{1:11}/\lambda^2\tilde{\eta}_0$. From the analysis presented in this paper, the values of these constants which best fit the rheology (§ 3.2), the shape transition (§ 3.8) and the terminal velocity (§ 3.10) are given in table 1.

The velocity and pressure fields of the drop interior are expanded as $\tilde{\boldsymbol{u}} = \tilde{\boldsymbol{u}}_0 + De\tilde{\boldsymbol{u}}_1 + De^2\tilde{\boldsymbol{u}}_2$ and $\tilde{p} = \tilde{p}_0 + De\tilde{p}_1 + De^2\tilde{p}_2$. This of course means that the deformation tensor is also written $\tilde{\boldsymbol{D}} = \tilde{\boldsymbol{D}}_0 + De\,\tilde{\boldsymbol{D}}_1 + De^2\tilde{\boldsymbol{D}}_2$. Note that the operator $\hat{\mathrm{d}}(\cdot)$ is also being perturbed, via its dependence on velocity, so that at each order

$$\hat{\mathrm{d}}_i(\cdot) = \left(\frac{\partial}{\partial t} + \tilde{\boldsymbol{u}}_i\cdot\nabla\right)(\cdot) - \nabla\tilde{\boldsymbol{u}}_i^T(\cdot) - (\cdot)\nabla\tilde{\boldsymbol{u}}_i.$$

Substituting these perturbations into (3.6) we obtain

$$\tilde{\boldsymbol{\tau}} = \tilde{\boldsymbol{\tau}}_0 + De\,\tilde{\boldsymbol{\tau}}_1 + De^2\,\tilde{\boldsymbol{\tau}}_2 + O(De^3) \tag{3.8}$$

where $\tilde{\boldsymbol{\tau}}_0 = 2\tilde{\boldsymbol{D}}_0$ is the zeroth-order Newtonian contribution, and

$$\tilde{\boldsymbol{\tau}}_1 = 2\tilde{\boldsymbol{D}}_1 - 2\hat{\mathrm{d}}_0\tilde{\boldsymbol{D}}_0 - 4B_{11}\tilde{\boldsymbol{D}}_0\cdot\tilde{\boldsymbol{D}}_0, \tag{3.9}$$

$$\begin{aligned}\tilde{\boldsymbol{\tau}}_2 = 2\tilde{\boldsymbol{D}}_2 - 2(\hat{\mathrm{d}}_0\tilde{\boldsymbol{D}}_1 + \hat{\mathrm{d}}_1\tilde{\boldsymbol{D}}_0) - 4B_{11}(\tilde{\boldsymbol{D}}_0\cdot\tilde{\boldsymbol{D}}_1 + \tilde{\boldsymbol{D}}_1\cdot\tilde{\boldsymbol{D}}_0) + 2B_3\hat{\mathrm{d}}_0^2\tilde{\boldsymbol{D}}_0 \\ + 4B_{12}(\hat{\mathrm{d}}_0\tilde{\boldsymbol{D}}_0\cdot\tilde{\boldsymbol{D}}_0 + \tilde{\boldsymbol{D}}_0\cdot\hat{\mathrm{d}}_0\tilde{\boldsymbol{D}}_0) + 8B_{1:11}(\tilde{\boldsymbol{D}}_0:\tilde{\boldsymbol{D}}_0)\tilde{\boldsymbol{D}}_0.\end{aligned} \tag{3.10}$$

https://doi.org/10.1017/S0022112003006621 Published online by Cambridge University Press

The elastic perturbations in the interior will also affect the exterior Newtonian flow, so we must similarly expand $\boldsymbol{u}$, p, and $\boldsymbol{\tau}$ in powers of De. At each order the stress tensor is $\boldsymbol{\tau}_i = (\nabla \boldsymbol{u}_i + \nabla \boldsymbol{u}_i^T)$.

Since both interior and exterior flows are incompressible and axisymmetric, we have the standard streamfunctions in spherical coordinates (Happel & Brenner 1965). The expansion of the velocity fields leads to

$$\psi = \psi_0 + De\,\psi_1 + De^2\,\psi_2,$$
$$\tilde{\psi} = \tilde{\psi}_0 + De\,\tilde{\psi}_1 + De^2\,\tilde{\psi}_2,$$

where at each order i

$$\boldsymbol{u}_i = \left(\frac{1}{r^2 \sin\theta} \frac{\partial \psi_i}{\partial \theta}, -\frac{1}{r \sin\theta} \frac{\partial \psi_i}{\partial r} \right)$$

and

$$\tilde{\boldsymbol{u}}_i = \left(\frac{1}{r^2 \sin\theta} \frac{\partial \tilde{\psi}_i}{\partial \theta}, -\frac{1}{r \sin\theta} \frac{\partial \tilde{\psi}_i}{\partial r} \right).$$

3.4. *Perturbative solutions*

We approach this problem by following the standard technique of perturbing the flow to a certain order, obtaining the solution for the flow that order, and then evaluating the forces on the boundary. The boundary shape is then adjusted in order to balance the forces, after which a domain perturbation (Joseph & Fosdick 1972) is done to recalculate the flow for this new shape (a higher-order correction).

By substituting the De expansions into the equations of motion, we find that both interior and exterior flows are driven Stokes flows at $O(1)$:

$$\nabla p_0 = \Delta \boldsymbol{u}_0 + \frac{\rho \boldsymbol{g} R^2}{\eta U_\infty}, \quad \nabla \tilde{p}_0 = \Delta \tilde{\boldsymbol{u}}_0 + \frac{\tilde{\rho} \boldsymbol{g} R^2}{\tilde{\eta}_0 U_0}.$$

To solve these equations, we substitute the streamfunctions for $\boldsymbol{u}_0, \tilde{\boldsymbol{u}}_0$ and eliminate pressure to obtain

$$\mathrm{E}^4 \psi_0 = 0, \quad \mathrm{E}^4 \tilde{\psi}_0 = 0,$$

where the operator $\mathrm{E}^4 \equiv \mathrm{E}^2 \mathrm{E}^2$ is defined by

$$\mathrm{E}^2 = \frac{\partial^2}{\partial r^2} + \frac{\sin\theta}{r^2} \frac{\partial}{\partial \theta} \left(\frac{1}{\sin\theta} \frac{\partial}{\partial \theta} \right).$$

Solutions of $\mathrm{E}^4 \Psi = 0$ are of the form (Happel & Brenner 1965)

$$\Psi = \sum_{n=1}^{\infty} \left(A_n r^{-n} + B_n r^{2-n} + C_n r^{n+1} + D_n r^{n+3} \right) Q_n(\mu) \tag{3.11}$$

where $\mu = \cos\theta$, and the Gegenbauer functions are

$$Q_n(\mu) = \int_{-1}^{\mu} P_n(x)\,\mathrm{d}x$$

with P_n the Legendre polynomial of degree n.

For the flow to remain finite, we have immediately in the exterior that $D_n = 0$ for all n, and $C_n = 0$ for $n \geqslant 2$; in the interior $A_n = B_n = 0$ for all n. Applying the interfacial

https://doi.org/10.1017/S0022112003006621 Published online by Cambridge University Press

boundary conditions at $r(\theta)=1$, we obtain the classic creeping flow solutions obtained by Hadamard (1911) and Rybczynski (1911):

$$\psi_0 = \frac{1}{4}\left(2r^2 - \frac{3\kappa+2}{\kappa+1}r + \frac{\kappa}{\kappa+1}\frac{1}{r}\right)\sin^2\theta,$$
$$\tilde{\psi}_0 = -\tfrac{1}{4}(r^2 - r^4)\sin^2\theta.$$

The interior streamfunction differs by a factor of $(\kappa+1)$ compared with Taylor & Acrivos (1964), due to our choice of non-dimensionalization. To compensate for the large viscosity difference, this choice was made so that both the flow at infinity and through the origin are $O(1)$.

Using these streamfunctions the velocity fields $\boldsymbol{u}_0$ and $\tilde{\boldsymbol{u}}_0$ can be calculated, from which the pressure fields p_0 and $\tilde{p}_0$ can also be determined. The overall forces on the drop (non-dimensionalized by $\eta R U_\infty$) are due to buoyancy and drag:

$$F = F_B + F_D = \frac{4\pi R^2(\rho-\tilde{\rho})g}{3\eta U_\infty} + 2\pi\left(\frac{3\kappa+2}{\kappa+1}\right). \tag{3.12}$$

Here we have utilized the Payne–Pell Theorem to calculate the drag force:

$$F_D = 8\pi \lim_{r\to\infty} \frac{\psi_\infty - \psi(r,\theta)}{r\sin^2\theta}, \tag{3.13}$$

where $\psi_\infty = (r^2\sin^2\theta)/2$ is the streamfunction for free streaming flow (Payne & Pell 1960). In steady state the forces balance ($F=0$ in (3.12)), which defines the Hadamard–Rybczynski terminal velocity:

$$U_\infty = U_{HR} \equiv \left(\frac{2\kappa+2}{9\kappa+6}\right)\frac{(\tilde{\rho}-\rho)gR^2}{\eta}. \tag{3.14}$$

To this point, we have not utilized the normal stress boundary condition (3.7). Evaluating the stress at the steady-state terminal velocity yields

$$\delta p = \frac{1}{Ca}\left(\frac{1}{R_1} + \frac{1}{R_2}\right),$$

where δp is the ambient pressure jump. When $R_1 = R_2 = 1$, we recover the standard Laplace pressure jump in non-dimensional form. In other words, a perfect sphere *is* a solution to the free boundary problem of creeping flow past a Stokes drop for non-zero Ca (Taylor & Acrivos 1964).

At all higher orders in De, the perturbations to the exterior flow are undriven Stokes flows: $\mathrm{E}^4\psi_i = 0$ for each i. However, both the shape of the drop boundary and the value of the boundary conditions will be different at each order.

For the interior flow at $O(De)$ we have

$$\nabla\tilde{p}_1 = \Delta\tilde{\boldsymbol{u}}_1 + \boldsymbol{f}_1(\tilde{\boldsymbol{u}}_0),$$
$$\boldsymbol{f}_1(\tilde{\boldsymbol{u}}_0) = -\nabla\cdot(\hat{\mathrm{d}}_0\,\tilde{\boldsymbol{D}}_0 + B_{11}\,\tilde{\boldsymbol{D}}_0\cdot\tilde{\boldsymbol{D}}_0).$$

Eliminating the pressure field in the usual way, we find

$$\mathrm{E}^4\tilde{\psi}_1 = r\sin\theta[\nabla\times\boldsymbol{f}_1(\tilde{\boldsymbol{u}}_0)]\cdot\boldsymbol{\delta}_\phi = 0.$$

https://doi.org/10.1017/S0022112003006621 Published online by Cambridge University Press

Applying the boundary conditions, we obtain

$$\psi_1 = \frac{(9-3B_{11})\kappa}{20(\kappa+1)^2}\left(\frac{1}{r^2}-1\right)\sin^2\theta\cos\theta,$$

$$\tilde{\psi}_1 = \frac{(9-3B_{11})\kappa}{20(\kappa+1)}(r^3-r^5)\sin^2\theta\cos\theta.$$

Using the full exterior streamfunction $\psi = \psi_0 + De\,\psi_1$ in (3.13), we find that there is no extra drag force contributed at $O(De)$. Thus the terminal velocity remains unchanged from the Hadamard–Rybczynski value, as was first seen for the viscoelastic drag on a rigid sphere by Leslie (1961), and later for a drop (Wagner & Slattery 1971).

3.5. *Deformation of the free boundary*

For $Ca = 0$, which corresponds to infinite surface tension, there will be no deformation. Likewise, because we are neglecting inertia, if De is zero there will be nothing to perturb the shape from spherical. Thus all perturbation terms must involve both De and Ca (Bird *et al.* 1987).

The non-dimensional perturbed boundary of the drop is given by the radius $r = 1+\zeta(\mu)$, where $\mu = \cos\theta$. For small deformations ($\max|\zeta| \ll 1$), Landau & Lifshitz (1959) showed that the total curvature can be approximated for the axisymmetric case as

$$\frac{1}{R_1}+\frac{1}{R_2} = 2-2\zeta-\frac{\mathrm{d}}{\mathrm{d}\mu}\left((1-\mu^2)\frac{\mathrm{d}\zeta}{\mathrm{d}\mu}\right). \tag{3.15}$$

The normal stress boundary condition (3.7) then becomes

$$\boldsymbol{n}\cdot\left(\boldsymbol{\tau}-\frac{\kappa}{\kappa+1}\tilde{\boldsymbol{\tau}}\right)\cdot\boldsymbol{n} - p + \tilde{p} = \frac{1}{Ca}\left(2-2\zeta-\frac{\mathrm{d}}{\mathrm{d}\mu}\left((1-\mu^2)\frac{\mathrm{d}\zeta}{\mathrm{d}\mu}\right)\right) \tag{3.16}$$

which allows the boundary to be expanded in De and Ca. Here we will assume that De and Ca are each of the order of a small parameter ϵ. The function ζ has to satisfy the two conditions

$$\int_{-1}^{1}\zeta\,\mathrm{d}\mu = 0, \quad \int_{-1}^{1}\zeta\,\mu\,\mathrm{d}\mu = 0. \tag{3.17}$$

These equations are respectively linearizations of the conditions that the volume of the drop must remain constant and that its centre of mass must remain at the origin. At the terminal velocity of the drop (3.14) we have

$$\delta p - 4\alpha_2 De P_2(\mu) = \frac{1}{Ca}\left(2-2\zeta-\frac{\mathrm{d}}{\mathrm{d}\mu}\left((1-\mu^2)\frac{\mathrm{d}\zeta}{\mathrm{d}\mu}\right)\right), \tag{3.18}$$

where

$$\alpha_2 = \frac{(56+74\kappa-17B_{11}-23\kappa B_{11})\kappa}{80(\kappa+1)^2}.$$

Solving with (3.17), we find that the boundary deformation is

$$\zeta = -\alpha_2 DeCa\;P_2(\cos\theta), \tag{3.19}$$

which is of the same form as the inertial correction found by Taylor & Acrivos (1964).

3.6. *Flow around the perturbed shape*

We will now perform a domain perturbation (Joseph & Fosdick 1972) to determine the effect of the deformed drop on the flow fields. We perturb the exterior and interior

https://doi.org/10.1017/S0022112003006621 Published online by Cambridge University Press

flows as

$$\boldsymbol{u} = \boldsymbol{u}^{(0)} + DeCa\boldsymbol{u}^{(1)}, \quad \tilde{\boldsymbol{u}} = \tilde{\boldsymbol{u}}^{(0)} + DeCa\tilde{\boldsymbol{u}}^{(1)},$$

where $\boldsymbol{u}^{(0)}$ and $\tilde{\boldsymbol{u}}^{(0)}$ are the previously obtained flow fields around the sphere. Interested only in terms up to $O(\epsilon^2)$, the new correction terms, $\boldsymbol{u}^{(1)}$ and $\tilde{\boldsymbol{u}}^{(1)}$, will each satisfy undriven Stokes equations. Thus we have

$$\mathrm{E}^4\psi^{(1)} = 0, \quad \mathrm{E}^4\tilde{\psi}^{(1)} = 0.$$

Rather than solving the boundary conditions on the surface of the drop $r(\theta) = 1 + \zeta(\cos\theta)$, we Taylor expand about the sphere $r(\theta) = 1$. Our interfacial boundary conditions (which will be evaluated at $r = 1$) become

$$\begin{aligned}
u_r^{(1)} - \alpha_2 P_2(\cos\theta)\frac{\partial u_{0,r}}{\partial r} - 3\alpha_2\cos\theta\sin\theta u_{0,\theta} &= 0,\\
\tilde{u}_r^{(1)} - \alpha_2 P_2(\cos\theta)\frac{\partial \tilde{u}_{0,r}}{\partial r} - 3\alpha_2\cos\theta\sin\theta \tilde{u}_{0,\theta} &= 0,\\
u_\theta^{(1)} - \alpha_2 P_2(\cos\theta)\frac{\partial u_{0,\theta}}{\partial r} + 3\alpha_2\cos\theta\sin\theta u_{0,r}&\\
= \frac{1}{\kappa+1}\left(\tilde{u}_\theta^{(1)} - \alpha_2 P_2(\cos\theta)\frac{\partial \tilde{u}_{0,\theta}}{\partial r} + 3\alpha_2\cos\theta\sin\theta\tilde{u}_{0,r}\right),&\\
\tau_{r\theta}^{(1)} - \alpha_2 P_2(\cos\theta)\frac{\partial \tau_{0,r\theta}}{\partial r} + 3\alpha_2\cos\theta\sin\theta(\tau_{0,rr} - \tau_{0,\theta\theta})&\\
= \frac{\kappa}{\kappa+1}\left(\tilde{\tau}_{r\theta}^{(1)} - \alpha_2 P_2(\cos\theta)\frac{\partial \tilde{\tau}_{0,r\theta}}{\partial r} + 3\alpha_2\cos\theta\sin\theta(\tilde{\tau}_{0,rr} - \tilde{\tau}_{0,\theta\theta})\right).&
\end{aligned}$$

Solving we obtain

$$\begin{aligned}
\psi^{(1)} &= \frac{\alpha_2}{10(\kappa+1)^2}\left((3\kappa^2 - \kappa + 8)r - \frac{3\kappa^2 - 3\kappa + 6}{r}\right)Q_1(\mu)\\
&\quad - \frac{3\alpha_2}{35(\kappa+1)}\left(\frac{21\kappa+18}{r} - \frac{21\kappa+4}{r^3}\right)Q_3(\mu),\\
\tilde{\psi}^{(1)} &= \frac{\alpha_2}{5(\kappa+1)}((4-2\kappa)r^4 + (3\kappa-3)r^2)Q_1(\mu) + \frac{6\alpha_2}{35}(5r^6 - 12r^4)Q_3(\mu).
\end{aligned}$$

As will be discussed in § 3.8, this flow will further perturb the boundary. Thus, we will need the $\boldsymbol{\tau}^{(1)}$ and $\tilde{\boldsymbol{\tau}}^{(1)}$ contributions to the normal stress boundary condition (3.16):

$$\begin{aligned}
\boldsymbol{n}\cdot\left(\boldsymbol{\tau}^{(1)} - \frac{\kappa}{\kappa+1}\tilde{\boldsymbol{\tau}}^{(1)}\right)\cdot\boldsymbol{n} &= \tau_{rr}^{(1)} - \alpha_2 P_2(\cos\theta)\frac{\partial \tau_{0,rr}}{\partial r} - 6\alpha_2\cos\theta\sin\theta\ \tau_{0,r\theta}\\
&\quad - \frac{\kappa}{\kappa+1}\left(\tilde{\tau}_{rr}^{(1)} - \alpha_2 P_2(\cos\theta)\frac{\partial \tilde{\tau}_{0,rr}}{\partial r} - 6\alpha_2\cos\theta\sin\theta\ \tilde{\tau}_{0,r\theta}\right). \quad (3.20)
\end{aligned}$$

3.7. *De^2 correction to the flow*

Since we have assumed that De and Ca are of the same order, and our perturbation of the boundary is $O(DeCa)$, we must also include terms of $O(De^2)$. We have in the interior

$$\begin{aligned}
\nabla\tilde{p}_2 &= \Delta\tilde{\boldsymbol{u}}_2 + \boldsymbol{f}_2(\tilde{\boldsymbol{u}}_0, \tilde{\boldsymbol{u}}_1)\\
\boldsymbol{f}_2(\tilde{\boldsymbol{u}}_0, \tilde{\boldsymbol{u}}_1) &= -\nabla\cdot((\hat{\mathrm{d}}_0\tilde{\boldsymbol{D}}_1 + \hat{\mathrm{d}}_1\tilde{\boldsymbol{D}}_0) + B_{11}(\tilde{\boldsymbol{D}}_0\cdot\tilde{\boldsymbol{D}}_1 + \tilde{\boldsymbol{D}}_1\cdot\tilde{\boldsymbol{D}}_0))\\
&\quad + \nabla\cdot(B_3\hat{\mathrm{d}}_0^2\tilde{\boldsymbol{D}}_0 + B_{12}(\hat{\mathrm{d}}_0\tilde{\boldsymbol{D}}_0\cdot\tilde{\boldsymbol{D}}_0 + \tilde{\boldsymbol{D}}_0\cdot\hat{\mathrm{d}}_0\tilde{\boldsymbol{D}}_0) + B_{1:11}(\tilde{\boldsymbol{D}}_0 : \tilde{\boldsymbol{D}}_0)\tilde{\boldsymbol{D}}_0).
\end{aligned}$$

https://doi.org/10.1017/S0022112003006621 Published online by Cambridge University Press

Thus in the interior we solve

$$\mathrm{E}^4\tilde{\psi}_2 = r\sin\theta[\nabla\times\boldsymbol{f}_2(\tilde{\boldsymbol{u}}_0,\tilde{\boldsymbol{u}}_1)]\cdot\boldsymbol{\delta}_\phi = -140a\,r^2\sin^2\theta, \tag{3.21}$$

where

$$a = -\frac{9\kappa}{100(\kappa+1)} + \frac{3\kappa}{25(\kappa+1)}B_{11} - \frac{3}{35}B_3 - \frac{63}{140}B_{12} + \frac{63}{140}B_{1:11}.$$

Noting that we solve these equations while evaluating the boundary conditions on a spherical drop, we have

$$\psi_2 = \frac{2a+c_1}{\kappa+1}\left(r-\frac{1}{r}\right)Q_1(\mu) + \frac{c_3}{\kappa+1}\left(\frac{1}{r}-\frac{1}{r^3}\right)Q_3(\mu),$$
$$\tilde{\psi}_2 = (a(r^6-r^2)+c_1(r^4-r^2))Q_1(\mu) + c_3(r^6-r^4)Q_3(\mu),$$

where

$$c_1 = \frac{9\kappa}{50(\kappa+1)} + \frac{3\kappa(\kappa-2)}{25(\kappa+1)^2}B_{11} - \frac{\kappa-12}{70(\kappa+1)}B_3 - \frac{9(\kappa-1)}{10(\kappa+1)}B_{12} + \frac{9(\kappa-1)}{10(\kappa+1)}B_{1:11},$$
$$c_3 = -\frac{531\kappa^2}{175(\kappa+1)^2} + \frac{321\kappa^2}{175(\kappa+1)^2}B_{11} + \frac{57\kappa}{35(\kappa+1)}B_3 - \frac{24\kappa}{35(\kappa+1)}B_{12} + \frac{9\kappa}{35(\kappa+1)}B_{1:11}.$$

3.8. *Drag and higher-order deformation*

The drag force on the drop, as perturbed according to the above analysis, can be calculated using (3.13) and the exterior streamfunction $\psi = \psi_0 + De\psi_1 + DeCa\psi^{(1)} + De^2\psi_2$ as

$$\begin{aligned}\frac{F_D}{2\pi} &= d_{0,0} + d_{1,1}DeCa + d_{2,0}De^2 \\ &= \frac{3\kappa+2}{\kappa+1} + \frac{3\kappa^2-\kappa+8}{5(\kappa+1)^2}\alpha_2 DeCa \\ &\quad + \frac{\kappa}{10(\kappa+1)^2}\left(\frac{12\kappa}{5(\kappa+1)}(3B_{11}-B_{11}^2) - \frac{26}{7}B_3 - 36B_{12} + 36B_{1:11}\right)De^2.\end{aligned} \tag{3.22}$$

Note that, as expected, the contribution from the shape change increases the drag (using the parameters in table 1), whereas the higher-order elastic effects decrease the drag, in agreement with Ramkissoon (1989).

From the balance of buoyancy and drag we have

$$U_\infty = \frac{2(\tilde{\rho}-\rho)gR^2}{3\eta(d_{0,0}+d_{1,1}DeCa+d_{2,0}De^2)}. \tag{3.23}$$

Inserting this terminal velocity and (3.20) into the the normal stress condition (3.16), we have

$$\begin{aligned}\delta p - 4\alpha_2 De\,P_2(\mu) - 10\beta_3 DeCa\,P_3(\mu) + 10\alpha_3 De^2 P_3(\mu) \\ = \frac{1}{Ca}\left(2-2\zeta - \frac{\mathrm{d}}{\mathrm{d}\mu}\left((1-\mu^2)\frac{\mathrm{d}\zeta}{\mathrm{d}\mu}\right)\right),\end{aligned} \tag{3.24}$$

where

$$\beta_3 = \frac{3(11\kappa+10)}{70(\kappa+1)}\alpha_2$$

https://doi.org/10.1017/S0022112003006621 Published online by Cambridge University Press

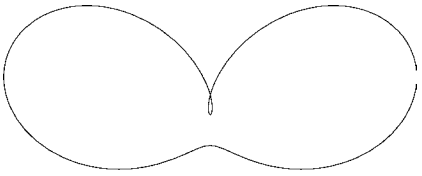


FIGURE 8. Theoretical prediction of the drop shape using the measured volume (1.4 ml) and velocity (1.6 cm s^{-1}) of the drop in figure 7(*a*). Note the unphysical cross-over of the boundary at the trailing edge of the falling drop.

and

$$\alpha_3 = \frac{\kappa}{350(\kappa+1)^2}\left(\frac{2937\kappa+3468\kappa^2}{10(\kappa+1)} - \frac{1621\kappa+1942\kappa^2}{10(\kappa+1)}B_{11} + \frac{107\kappa+131\kappa^2}{5(\kappa+1)}B_{11}^2 - \frac{437+494\kappa}{2}B_3 + (71+83\kappa)B_{12} - \frac{27+36\kappa}{2}B_{1:11}\right).$$

Solving with (3.17) for ζ, we find that the axisymmetric boundary is given by

$$r(\theta) = 1 - \alpha_2 Ca\,De\,P_2(\cos\theta) - \beta_3 Ca^2\,De\,P_3(\cos\theta) + \alpha_3 Ca\,De^2\,P_3(\cos\theta). \tag{3.25}$$

Using the measured terminal velocity of the drops in figure 4 to calculate De and Ca, we obtain a theoretical prediction of the shapes using the parameter values listed in table 1, as shown in figure 5.

3.9. *The model beyond its limits*

Since we are making an expansion, ideally we would like the parameters De and Ca to be small. Thus it is intriguing that we were able to qualitatively capture the shapes of the drops in figure 4, although the drop of volume 0.5 ml has $De \simeq 1$ and $Ca \simeq 0.5$. If we push our model further by computing the shape of a drop nearly three times this size, our theory predicts that the boundary will self-intersect at the trailing edge of the drop (see figure 8). However, as unphysical as this result appears, it may correspond to the experimental observation of internal pinch-off at this location (figure 7*a*).

Here there is a surprising correlation with ocean surface waves. From an exact solution, Crapper (1957) was able to determine the greatest height of capillary waves. When his solution is pushed further, the surface also self-intersects, which was used to predict the entrainment of air bubbles in the wave troughs (Longuet-Higgins 1988).

3.10. *Discussion of terminal velocity*

Originally we non-dimensionalized the external velocity field by the drop's terminal velocity U_∞. However the drop's terminal velocity is an easily measured quantity, and by studying U_∞ it is possible to compare experiments with different fluids or drop sizes. First, by solving (3.23) for velocity in the limit of zero De, we get the Hadamard–Rybczynski velocity (3.14). Combining this with (3.23), we can obtain the departure of U_∞ from U_{HR} due to non-Newtonian effects:

$$U_\infty = \frac{d_{0,0}}{d_{0,0} + d_{1,1}DeCa + d_{2,0}De^2}\,U_{HR}. \tag{3.26}$$

Since our control parameters, De and Ca, are also functions of U_∞, we must solve this equation implicitly to find the terminal velocity of the drop. Using the parameters in table 1, we plot U_∞ vs. R in figure 6 along with the experimental data.

https://doi.org/10.1017/S0022112003006621 Published online by Cambridge University Press

4. Conclusions

In this paper we have presented the first experimental observation of a non-Newtonian drop falling through a viscous Newtonian fluid, using an elastic polymer solution (xanthan gum) as the drop phase. As the volume of the drop is increased, the primary transition of the free boundary from its spherical shape is due to non-Newtonian effects; inertial effects remain negligible. We observe the transition to a dimpled shape, similar to the well-known inertial instability to a dimpled drop (Wellek *et al.* 1966). Our analysis uses a perturbation expansion about the classic Hadamard–Rybczynski solution. Using the constitutive equation for a Simple Fluid of Order Three, we have successfully reproduced the main aspects of the steady-state shape and velocity of the drop while also fitting the gross features of the shear rheology.

Beyond the validity of this expansion, we have experimentally observed the shape of larger polymer drops. Two new instabilities have been observed as the volume is further increased. One is the extension of the interior cusp into a pendant drop followed by a filament, which becomes unstable via a Rayleigh-type instability to many smaller droplets. For even larger volumes, stable toroidal drops are observed, the result of the elastic stress in the polymer solution overcoming surface tension.

In viscous flows, steady free-surface shapes such as the cusp-like tail of a rising air bubble (Hassager 1979; Liu *et al.* 1995) or the dimpled drop observed here, seem to require non-Newtonian effects. However, drops with large and transient tails or dimples are seen in viscous Newtonian fluids, as a result of either finite initial perturbations or the absence of surface tension (Koh & Leal 1989, 1990; Pozrikidis 1990). This similarity between the transient Newtonian and the steady non-Newtonian shapes may be indicative of a deeper mathematical connection between these free-boundary problems.

We would like to thank T. Podgorski for valuable discussions and critical reading of the manuscript, J. Hammack and D. M. Henderson for pointing out the connection to air entrainment in capillary waves, and R. Geist for experimental assistance. This work was supported by the A. P. Sloan Foundation and National Science Foundation (CAREER Award DMR-0094167).

REFERENCES

Ambwani, D. S. & Fort, T. 1979 Pendant drop technique for measuring liquid boundary tensions. In *Surface and Colloid Science, Vol. 11. Experimental Methods* (ed. R. J. Good & R. R. Stromberg), pp. 93–118. Plenum.

Batchelor, G. K. 1967 *An Introduction to Fluid Dynamics*. Cambridge University.

Baumann, N., Joseph, D. D., Mohr, P. & Renardy, Y. 1992 Vortex rings of one fluid in another in free fall. *Phys. Fluids* A **4**, 567–580.

Benjamin, T. B. & Ellis, A. T. 1966 The collapse of cavitation bubbles and the pressures thereby produced against solid boundaries. *Phil. Trans. R. Soc. Lond.* A **260**, 221–240.

Bird, R. B., Armstrong, R. C. & Hassager, O. 1987 *Dynamics of Polymeric Liquids, Vol. 1*, 2nd Edn. Wiley-Interscience.

Boger, D. V. & Walters, K. 1993 *Rheological Phenomena in Focus*. Elsevier.

Caswell, B. & Schwarz, W. H. 1962 The creeping motion of a non-Newtonian fluid past a sphere. *J. Fluid Mech.* **13**, 417–426.

Crapper, G. D. 1957 An exact solution for progressive capillary waves of arbitrary amplitude. *J. Fluid Mech.* **2**, 532–540.

Dairenieh, L. S. & McHugh, A. J. 1985 Viscoelastic fluid flow past a submerged spheroidal body. *J. Non-Newtonian Fluid Mech.* **19**, 81–111.

https://doi.org/10.1017/S0022112003006621 Published online by Cambridge University Press

Eggers, J. 1997 Nonlinear dynamics and breakup of free-surface flows. *Rev. Mod. Phys.* **69**, 865–929.

Garner, F. H., Mathur, K. B. & Jenson, V. G. 1957 Distortion of fluid drops in the Stokesian regime. *Nature* **180**, 331–332.

Goldin, M., Yerushalmi, J., Pfeffer, R. & Shinnar, R. 1969 Breakup of a laminar capillary jet of a viscoelastic fluid. *J. Fluid Mech.* **38**, 689–711.

Hadamard, J. 1911 Mouvement permanent lent d'une sphere liquide et visqueuse dans un liquide visqueux. *C. R. Acad. Sci. Paris* **152**, 1735–1738.

Happel, J. & Brenner, H. 1965 *Low Reynolds Number Hydrodynamics*. Prentice-Hall.

Hassager, O. 1979 Negative wake behind bubbles in non-Newtonian liquids. *Nature* **279**, 402–403.

Jeong, J. & Moffatt, H. K. 1992 Free-surface cusps associated with flow at low Reynolds number. *J. Fluid Mech.* **241**, 1–22.

Joseph, D. D. & Fosdick, R. L. 1972 The free surface on a liquid between cylinders rotating at different speeds. Part 1. *Arch. Rat. Mech. Anal.* **49**, 321–350.

Koh, C. J. & Leal, L. G. 1989 The stability of drop shapes for translation at zero Reynolds number through a quiescent fluid. *Phys. Fluids* A **1**, 1309–1313.

Koh, C. J. & Leal, L. G. 1990 An experimental investigation on the stability of viscous drops translating through a quiescent fluid. *Phys. Fluids* A **2**, 2103–2109.

Kojima, M., Hinch, E. J. & Acrivos, A. 1984 The formation and expansion of a toroidal drop moving in a viscous fluid. *Phys. Fluids* **27**, 19–32.

Kushner, J., Rother, M. A. & Davis, R. H. 2001 Buoyancy-driven interactions of viscous drops with deforming interfaces. *J. Fluid Mech.* **446**, 253–269.

Landau, L. & Lifshitz, I. 1959 *Fluid Mechanics*. Pergamon.

Larson, R. G. 1992 Instabilities in viscoelastic flows. *Rheol. Acta* **31**, 213–263.

Leslie, F. M. 1961 The slow flow of a viscoelastic liquid past a sphere. *Q. J. Mech. Appl. Maths* **14**, 36–48.

Liu, Y., Liao, T. & Joseph, D. D. 1995 A two-dimensional cusp at the trailing edge of an air bubble rising in a viscoelastic liquid. *J. Fluid Mech.* **304**, 321–342.

Longuet-Higgins, M. S. 1988 Limiting forms of capillary-gravity waves. *J. Fluid Mech.* **194**, 351–375.

Machu, G., Meile, W., Nitsche, L. C. & Schaflinger, U. 2001 Coalescence, torus formation, and breakup of sedimenting drops: experiments and computer simulations. *J. Fluid Mech.* **447**, 299–336.

Marten, K., Shariff, K., Psarakos, S. & White, D. J. 1996 Ring bubbles of dolphins. *Sci. Am.* **275**, 82–87.

Milliken, W. J. & Leal, L. G. 1991 Deformation and breakup of viscoelastic drops in planar extensional flows. *J. Non-Newtonian Fluid Mech.* **40**, 355–379.

Nussinovitch, A. 1997 *Hydrocolloid Applications*. Blackie Academic & Professional.

Payne, L. E. & Pell, W. H. 1960 The Stokes flow problem for a class of axially symmetric bodies. *J. Fluid Mech.* **7**, 529–342.

Pozrikidis, C. 1990 The instability of a moving viscous drop. *J. Fluid Mech.* **210**, 1–21.

Ramkissoon, H. 1989 Stokes flow past a Reiner-Rivlin liquid sphere. *Z. Angew. Math. Mech.* **69**, 259–261.

Ramkissoon, H. 1998 Stokes flow past a non-Newtonian fluid spheroid. *Z. Angew. Math. Mech.* **78**, 61–66.

Rybczynski, W. 1911 Über die fortschreitende Bewegung einer flüssigen Kugel in einem zähen Medium. *Bull. Acad. Sci. de Cracovie* **A**, 40–46.

Shaqfeh, E. S. G. 1996 Purely elastic instabilities in viscometric flows. *Annu. Rev. Fluid Mech.* **28**, 129–185.

Shi, X. D., Brenner, M. P. & Nagel, S. R. 1994 A cascade of structure in a drop falling from a faucet. *Science* **265**, 219–222.

Smolka, L. B. & Belmonte, A. 2000 Effects of salt on filament dynamics during drop pinch-off in xanthan gum solutions. *Phys. Fluids* (submitted).

Stone, H. A. 1994 Dynamics of drop deformation and breakup in viscous fluids. *Annu. Rev. Fluid Mech.* **26**, 65–102.

Taylor, G. I. 1934 The formation of emulsions in definable fields of flow. *Proc. R. Soc. Lond.* A **146**, 501–523.

https://doi.org/10.1017/S0022112003006621 Published online by Cambridge University Press

Taylor, T. D. & Acrivos, A. 1964 On the deformation and drag of a falling viscous drop at low Reynolds number. *J. Fluid Mech.* **18**, 466–476.

Tiefenbruck, G. F. & Leal, L. G. 1980 A note on the slow motion of a bubble in a viscoelastic liquid. *J. Non-Newtonian Fluid Mech.* **7**, 257–264.

Venet, C. & Vergnes, B. 1997 Experimental characterization of sharkskin in polyethylenes. *J. Rheol.* **41**, 873–892.

Wagner, M. G. & Slattery, J. C. 1971 Slow flow of a non-Newtonian fluids past a droplet. *AIChE J.* **17**, 1198–1207.

Walters, J. K. & Davidson, J. F. 1963 The initial motion of a gas bubble formed in an inviscid liquid. Part 2. The three-dimensional bubble and the toroidal bubble. *J. Fluid Mech.* **17**, 321–336.

Wellek, R. M., Agrawal, A. K. & Skelland, A. H. 1966 Shape of liquid drops moving in liquid media. *AIChE J.* **12**, 854–862.

Whitcomb, P. J. & Macosko, C. W. 1978 Rheology of xanthan gum. *J. Rheol.* **22**, 493–505.

https://doi.org/10.1017/S0022112003006621 Published online by Cambridge University Press